



Au@Cu₂O core@shell nanocrystals as sustainable catalysts for efficient hydrogen production from ammonia borane

Mei-Jing Fang^a, Yu-Chang Lin^b, Jen-Yu Jan^c, Ting-Hsuan Lai^a, Ping-Yen Hsieh^a,
Ming-Yu Kuo^a, Yi-Hsuan Chiu^a, Chun-Wen Tsao^a, Yi-An Chen^a, Yu-Ting Wang^a,
Yi-Jia Hong^{a,b}, Jhen-Yang Wu^d, Yew Chung Sermon Wu^a, Yan-Gu Lin^b, Tso-Fu Mark Chang^d,
Chun-Yi Chen^d, Masato Sone^d, Sue-Min Chang^c, Chung-Liang Chang^e, Yung-Jung Hsu^{a,f,g,*}

^a Department of Materials Science and Engineering, National Yang Ming Chiao Tung University, Hsinchu 300093, Taiwan

^b National Synchrotron Radiation Research Center, Hsinchu 30076, Taiwan

^c Institute of Environmental Engineering, National Yang Ming Chiao Tung University, 1001 University Road, Hsinchu 300093, Taiwan

^d Institute of Innovative Research, Tokyo Institute of Technology, Kanagawa 226-8503, Japan

^e Department of Environmental Engineering and Health, Yuanpei University of Medical Technology, Hsinchu 30015, Taiwan

^f Center for Emergent Functional Matter Science, National Yang Ming Chiao Tung University, Hsinchu 300093, Taiwan

^g International Research Frontiers Initiative, Institute of Innovative Research, Tokyo Institute of Technology, Kanagawa 226-8503, Japan

ARTICLE INFO

Keywords:

Au@Cu₂O
Core@shell
Hydrogen production
Ammonia borane
Hydrolysis
Light emitting diodes

ABSTRACT

The use of Au@Cu₂O core@shell nanocrystals as sustainable catalysts for efficient hydrogen (H₂) production from ammonia borane (AB) is demonstrated. By combining the attributes associated with core@shell structural features and electronic interactions, Au@Cu₂O exhibited remarkable performance toward AB hydrolysis. The effect of shell thickness on H₂ production performance was systematically investigated. Results showed that H₂ production rate increased monotonically with shell thickness, while degree of dehydrogenation of AB was subject to optimization by shell thickness. A maximal 3.0 equivalents of H₂ production can be achieved by Au@Cu₂O with an optimal Cu₂O shell thickness. The H₂ produced from AB hydrolysis on Au@Cu₂O was introduced to power a fuel cell for lightening light emitting diodes. The findings from the work not only enrich the family of metal/metal oxide composite catalysts for AB hydrolysis, but also deepen the fundamental understanding of implications of core@shell structural features and electronic interactions in dehydrogenation of AB.

1. Introduction

The ever-rising energy crisis resulting from the excessive use of fossil fuels have instigated the scientists for the exploration of an alternative energy source that can accomplish the demand of energy scarcity. To this end, interests have peaked in exploiting renewable energy resources, such as sunlight, wind, waves, biomass and hydrogen (H₂). Among the accessible environmentally friendly resources, H₂ is considered as clean alternative to fossil fuels because its combustion merely produces water that can be reused to achieve a recycle process [1–3]. Obtaining H₂ from catalyzing H₂ storage materials is regarded as a facile and effective approach to construct a conceptual model for H₂ energy. Ammonia borane (denoted as AB), which has a high H₂ gravimetric capacity (19.6 wt%) yet a low molecular weight (30.9 g mol⁻¹), is a stable H₂ storage material under ambient temperature at both solid

powder form and aqueous solution [4]. Releasing H₂ from AB by heterogeneous catalysis has been in the limelight of H₂ economic outlook because of its potential viability for on-demand transportation applications. Efforts have been devoted to the creation of sustainable catalysts that can catalyze the dehydrogenation of AB to achieve efficient H₂ release under ambient conditions. Three distinct approaches have been proposed and realized to release H₂ from AB, including pyrolysis, alcoholysis and hydrolysis [5,6]. Among them, hydrolysis is the simplest route without the need of high-temperature operation or the production of organic byproducts. In practice, one mole of AB can generate up to three moles of H₂ under ambient conditions with the use of suitable catalysts. Since Xu's pioneering work in 2006 [7], many precious metal-based (Pt, Ru, Rh and Au) [7–12] and non-precious metal-based (Fe, Co, Ni and Cu) [13–16] catalysts have been designed for realizing H₂ release from AB hydrolysis. Besides metals, metal oxides (Cu₂O,

* Corresponding author at: Department of Materials Science and Engineering, National Yang Ming Chiao Tung University, Hsinchu 300093, Taiwan.
E-mail addresses: yhsu@nycu.edu.tw, yhsu@cc.nctu.edu.tw (Y.-J. Hsu).

Co_3O_4 , and WO_3) can serve as practical catalysts to release H_2 from AB hydrolysis [16–18]. Some other metal oxides (CeO_2 and SiO_2) can function as supporting substrates to immobilize and disperse metal particle catalysts, stabilizing the long-term catalytic activity as well [19, 20].

Recent focus has been put on the creation of multi-component catalysts for boosting the performance of H_2 production from AB hydrolysis. Attempts have been mostly made on the design of sophisticated metal-based catalysts by integrating multiple components into a unique architecture [21–23]. The core concept is modulating the electronic structure of the active component in an interest of facilitating the interaction with AB molecules. On the other hand, integrating metal particles with metal oxide structures has also proven effective in the design of composite catalysts for enhanced AB hydrolysis. The strategy lies behind the principle of using metal oxide structures to protect metal particles from agglomeration during the catalytic reaction process [18]. In addition to the rapid and prosperous development on the design of multi-component metallic catalysts, the advancement of composite catalysts comprising metals and metal oxides has also been dynamic. Previous studies ever developed several kinds of metal/metal oxide composite catalysts for AB hydrolysis, including Au- $\text{WO}_{2.72}$ [24], Au/ TiO_2 [25], Pt/ MoO_{3-x} [26], Cu@ Cu_2O [16], Cu/ Co_3O_4 [17] and Pt- WO_3 [18]. These works were mostly designed to highlight the advantage of combining metal with metal oxide as a composite catalyst and explore the influence of structural parameters, constituent compositions and catalysts preparation conditions on the catalytic performance. For example, in the study on Au- $\text{WO}_{2.72}$ [24], introducing 2 wt% Au was found to largely enhance the H_2 production performance of $\text{WO}_{2.72}$, revealing the beneficial catalytic feature of Au- $\text{WO}_{2.72}$. Similarly, the study on Cu@ Cu_2O demonstrated its superior activity to Cu in H_2 production from AB hydrolysis [16]. In the study on Au/ TiO_2 [25], the concentration of Au was adjusted from 0.5 to 3 wt% to evaluate the optimal Au content for achieving the highest H_2 production activity. In the study on Pt/ MoO_{3-x} [10], the catalysts were prepared under different calcination temperatures to evaluate its implication in AB hydrolysis. In the other study on Cu/ Co_3O_4 [17], the content of Cu and the morphology of Co_3O_4 were modulated in order to acquire the best experimental conditions, and thereby create a highly active and robust catalyst. It is important to highlight that the electronic interactions between metals and metal oxides are supposed to be significant, which have however not been exploited to tailor the catalytic properties yet. Therefore, it is extremely craving to search for versatile metal/metal oxide composite catalysts with an aim to modulate the electronic properties so as to enhance the performance of H_2 production from AB hydrolysis.

In this work, we employed Au@ Cu_2O core@shell nanocrystals as a sustainable catalyst for H_2 production from AB hydrolysis. Note that Au@ Cu_2O possessed many advantages for dehydrogenation of AB by virtue of the core@shell architecture. First, the Au core particles were encapsulated in the Cu_2O shell, preventing them from aggregation during the catalytic reaction. A long-term stability for efficient AB hydrolysis can be expected for Au@ Cu_2O . Second, not only the core Au was intrinsically active toward AB hydrolysis, but also the shell Cu_2O was effective in catalyzing the dehydrogenation of AB. The electronic interplay between the Au core and Cu_2O shell may give rise to synergistic effect to enhance the overall catalytic performance. Literature reports on AB hydrolysis over the past decade usually used noble metals and transition metals as metallic catalysts. Even though Au did not exhibit particularly remarkable activity, its relatively high inertness could guarantee high chemical robustness during the catalytic reaction process. Much significantly, the substantially higher work function of Au relative to other commonly used metals can elicit more pronounced electronic interactions with Cu_2O , which can be made use of to modulate the catalytic properties. By combining the attributes associated with the structural regulation and electronic engineering, Au@ Cu_2O was expected to exhibit remarkable catalytic performance toward AB

hydrolysis. The current study has delivered the first success of using Au@ Cu_2O core@shell nanocrystals as a sustainable catalyst for H_2 production from AB hydrolysis. The findings from this work can convey valuable information from both scientific and practical points of view.

2. Material and methods

2.1. Chemicals

All chemicals were obtained from Sigma-Aldrich, including copper (II) sulfate hydrate ($\text{CuSO}_4 \cdot 5\text{H}_2\text{O}$), sodium hydroxide (NaOH), L-ascorbic acid ($\text{C}_6\text{H}_8\text{O}_6$, denoted as LAA), salicylic acid ($\text{C}_7\text{H}_6\text{O}_3$, 99.5 %), sodium citrate dehydrate ($\text{C}_6\text{H}_5\text{Na}_3\text{O}_7 \cdot 2\text{H}_2\text{O}$, 99.0 %), sodium hypochlorite (NaClO, 4 % available chlorine), sodium nitroferrocyanide dihydrate ($\text{C}_5\text{FeN}_6\text{Na}_2\text{O} \cdot 2\text{H}_2\text{O}$, 99 %), and ammonia borane (NH_3BH_3 , denoted as AB, purity $\geq 97\%$), were analytical grade and used without further purification. Deionized water was used as solvent in synthesis.

2.2. Preparation of Au@ Cu_2O

Au particle colloids (0.25 mM) were first obtained from the typical citrate reduction method. To deposit Cu_2O on Au [27], two solutions were prepared. A given amount of CuSO_4 solution (10 mM, 2.0 mL) was mixed with deionized water (13.0 mL) in a two-neck round-bottom flask. Another mixed solution containing 1.5 mL of NaOH (1 M), 0.5 mL of LAA (100 mM) and 21.5 mL of deionized water was prepared in a vial. Afterwards, the Au colloids were added to the CuSO_4 solution, followed by a quick injection of the mixed solution of NaOH and LAA. Upon steadily stirred at 35 °C for 10 min, the samples (Au@ Cu_2O) were collected by centrifugation. By adjusting the volume of the added Au colloids (4.0, 3.0, 2.0, 1.0 mL), Au@ Cu_2O with four different shell thicknesses can be obtained. The products were respectively denoted as 4-Au@ Cu_2O , 3-Au@ Cu_2O , 2-Au@ Cu_2O , 1-Au@ Cu_2O . Three additional control samples were also synthesized. Pure Cu_2O nanocrystals with a particle size approximating to 2-Au@ Cu_2O were prepared by using the same synthetic method without the addition of Au. Pure Au particle precipitate was obtained by drying the precipitate collected from the centrifugation of Au colloids. Furthermore, Au@Cu core@shell nanocrystals were synthesized by deliberately conducting chemical reduction on 2-Au@ Cu_2O using N_2H_4 as reducing agent [28].

2.3. Characterizations

X-ray powder diffraction (XRD) patterns (Bruker, D2 Phaser) were recorded to examine the composition and crystallinity of the samples. UV-visible absorption spectra were measured (U3900H, Hitachi) to study the optical properties. Steady-state photoluminescence (PL) spectra were recorded (Hitachi, F-4500) to explore the electronic state of the samples. A field-emission scanning electron microscope (SEM, Hitachi, SU-8010) was used to characterize the morphology and dimension. A scanning transmission electron microscope (STEM, JEOL, JEM-ARM200FTH) equipped with a spherical-aberration corrector and high angle annular dark field (HAADF) detector was used to examine the atomic structure. Selected-area electron diffraction (SAED) and energy dispersive X-ray spectrometer (EDS) equipped on the STEM were used to investigate the detailed crystallographic structure and elemental distribution. Brunauer-Emmett-Teller (BET) surface areas were determined from the N_2 adsorption-desorption isotherms (Micromeritics ASAP2020). X-ray photoelectron (XPS, Thermo Fisher Scientific, ESCALAB Xi+) analysis with Al K α radiation was performed to acquire the chemical states. To determine the band structure, ultraviolet photoelectron spectroscopy (UPS, ULVAC-PHI PHI 5000 Versaprobe II) measurements using He I excitation ($h\nu = 21.22\text{ eV}$) were conducted. A Fourier-transform infrared spectroscopy (FTIR, Bruker, Tensor 27) equipped with an optical path gas cell (PIKE Technologies, Model#2.4-PA) was utilized to analyze the liberated NH_3 in the gas product from AB

hydrolysis over 2-Au@Cu₂O. The characteristic absorption peak at 966 cm⁻¹ was monitored to calibrate the concentration of NH₃.

2.4. AB hydrolysis

The performance of hydrolysis of AB on Au@Cu₂O was examined by collecting the evolved H₂ gas by downward displacement of water. In a typical procedure, a given amount of catalysts was added to the AB solution (5.0 mL, 60 mM) in an airtight flask equipped with a deliver tube connecting with a water-filled test tube. The amount of the H₂ evolved was then determined from the headspace of the test tube where the gas occupied. Measurements were taken at 313 K every 5 min over a 60 min interval. Note that the particle number of the four Au@Cu₂O catalysts was kept the same in order to fix the amount of Au and study the influence of the shell thickness. The added weight was 3.00, 3.75, 6.46, and 11.56 mg for 4-Au@Cu₂O, 3-Au@Cu₂O, 2-Au@Cu₂O, 1-Au@Cu₂O, respectively, which corresponded to an equivalent particle number of 7.63×10^{12} . Detailed calculations for particle number can be found in [supplementary material](#). Recycling tests were conducted by performing AB hydrolysis for ten repeated cycles under the same experimental condition. After each cycle, the catalyst powder was centrifuged, washed with distilled water, and loaded into the flask filled with fresh AB to carry out the catalysis.

2.5. PL quenching of pyrene

To explore the electronic state of Au@Cu₂O, PL quenching experiments by using pyrene as a chromogenic reagent were performed [29]. Briefly, a pyrene solution (2.0 mL, 6.25 μM) was added to an ethanol solution (2.0 mL) containing Au@Cu₂O with the same amount as that used in AB hydrolysis. After steadily stirred for 10 min, the mixed solution was analyzed with steady-state PL spectroscopy. The PL spectra of pyrene were recorded at the emission wavelength range from 350 to 450 nm. The excitation wavelength was set at 317 nm.

2.6. Soft X-ray absorption spectroscopy

X-ray absorption near edge structure (XANES) technique was used to elucidate the local electronic structure of the selected atoms. Soft X-ray absorption spectra (XAS) were measured in both total fluorescence-yield (TFY) and total electron-yield (TEY) modes at beamline TLS 20 A at the National Synchrotron Radiation Research Center in Hsinchu, Taiwan. The spectra in TFY and TEY modes were recorded simultaneously during the measurements.

2.7. Quantification of NH₄⁺

A colorimetric indophenol blue method [30] was employed to quantify the concentration of the generated NH₄⁺ in the liquid product from AB hydrolysis. In a typical procedure, 2.0 mL of the reaction solution from AB hydrolysis over 2-Au@Cu₂O was sampled after the hydrolysis reaction was completed. Subsequently, a NaOH solution (2.0 mL, 1.0 M) containing 5.0 wt% C₇H₆O₃ and 5.0 wt% C₆H₅Na₃O₇, a NaClO solution (1.0 mL, 0.05 M) and a C₅FeN₆Na₂O solution (0.2 mL, 1.0 wt%) were successively added to the sampled solution. The absorption spectrum of the mixed solution was recorded. The characteristic absorption peak around 652 nm was monitored to calibrate the concentration of NH₄⁺.

3. Results and discussion

3.1. Microstructure and chemical compositions

The synthesis of Au@Cu₂O relied on the linkage between Cu²⁺ and Au where the surface was protected by citrate. By virtue of the binding capability of the citrate ligands, Cu₂O can be uniformly deposited on the

Au particle surface, producing Au@Cu₂O core@shell nanocrystals with a high structural integrity. As shown in [Fig. 1](#), the TEM images clearly revealed the core@shell morphology for each of the sampled nanocrystals. Different from the previous work where the Cu₂O shell thickness was controlled by adjusting the concentration of Cu²⁺, the present study employed various contents of the added Au particles at a fixed Cu²⁺ concentration to achieve the shell thickness control for Au@Cu₂O. This modified approach led to the production of Au@Cu₂O with an improved uniformity and extensive growth in shell thickness. The resultant shell thickness of 4-Au@Cu₂O, 3-Au@Cu₂O, 2-Au@Cu₂O, and 1-Au@Cu₂O was respectively 17.0 ± 1.0 , 19.0 ± 1.3 , 24.5 ± 1.3 and 31.5 ± 1.9 nm. It is important to mention that the reported shell thickness values for the four Au@Cu₂O were based on the statistical results of particle size distribution by counting over 100 individual particles from a set of TEM images. [Fig. S1 \(supplementary material\)](#) displayed how the particle size distribution was obtained by counting individual particles from a TEM image for two representative samples. For each Au@Cu₂O samples, 8–10 separate TEM images containing over 100 individual particles were necessary to obtain reliable statistical data. As summarized in [Fig. S2 \(supplementary material\)](#), the particle size of 4-Au@Cu₂O, 3-Au@Cu₂O, 2-Au@Cu₂O and 1-Au@Cu₂O was respectively determined to be 49.0 ± 1.0 , 53.0 ± 1.3 , 64.0 ± 1.3 and 78.0 ± 1.9 nm. By subtracting the size of Au core (15.0 nm) from the particle size, the shell thickness value can be estimated, giving 17.0 ± 1.0 , 19.0 ± 1.3 , 24.5 ± 1.3 and 31.5 ± 1.9 nm for 4-Au@Cu₂O, 3-Au@Cu₂O, 2-Au@Cu₂O and 1-Au@Cu₂O, respectively. Note that Au served as the core for Cu₂O deposition. Under a situation of a fixed Cu²⁺ concentration, addition of less Au particles would result in more Cu₂O deposition, leading to an increase in Cu₂O shell for Au@Cu₂O. As a control sample, pure Cu₂O nanocrystals were also prepared by using the same synthetic method without the addition of Au. By adjusting the synthetic condition, the diameter of pure Cu₂O was tuned to approximate to the particle size of 2-Au@Cu₂O, which was 67.0 ± 6.8 nm as determined from [Fig. S3\(a\) \(supplementary material\)](#). In [Fig. S3\(b\) \(supplementary material\)](#), pure Au particle precipitate was also analyzed, showing particle agglomeration with a primary size of around 15.0 nm. To further characterize the microstructural features of Au@Cu₂O, high-resolution TEM, SAED, STEM-HAADF imaging and TEM-EDS mapping analysis were conducted. As shown in [Fig. 2\(a\)](#), the recorded d-spacings of 0.24, 0.21 and 0.15 nm corresponded to the (111), (200) and (220) planes of cubic Cu₂O, while the obtained distances of 0.23 and 0.20 nm reflected the (111) and (200) planes of fcc Au, respectively. The SAED pattern in [Fig. 2\(b\)](#) displayed two distinct sets of ring patterns that can be assigned to the characteristic diffraction planes of cubic Cu₂O and fcc Au. The STEM-HAADF image of [Fig. 2\(c\)](#) clearly revealed the spatially-resolved, rigid heterojunctions between the inner core and outer shell. The EDS mapping data further showed that the Cu and O elements were uniformly distributed throughout the nanocrystal, whereas Au element was mainly present in the middle of the structure, suggesting the shell composition as Cu₂O and the core composition as Au. The content of Cu₂O can be estimated from the SEM-EDS analytical results. As summarized in [Fig. S4 and Table S1 \(supplementary material\)](#), the content of Cu₂O was respectively 90.16, 93.39, 95.16 and 97.57 mol% for 4-Au@Cu₂O, 3-Au@Cu₂O, 2-Au@Cu₂O and 1-Au@Cu₂O.

The chemical compositions of the samples were further analyzed with XRD and UV–visible absorption. In [Fig. 3\(a\)](#), the XRD patterns of the four Au@Cu₂O revealed the existence of cubic Cu₂O and fcc Au. As the shell thickness increased, the relative peak intensity of Cu₂O increased. The pattern of pure Cu₂O was also collected, showing the constituent component of cubic Cu₂O. With similar microstructural feature and identical crystallographic structure to 2-Au@Cu₂O, pure Cu₂O can serve as a righteous control sample for performance comparison in order to reveal the influence of Au core. The constituent components of Au and Cu₂O can also be explored with UV–visible absorption spectroscopy. [Fig. 3\(b\)](#) compares the UV–visible absorption spectra for

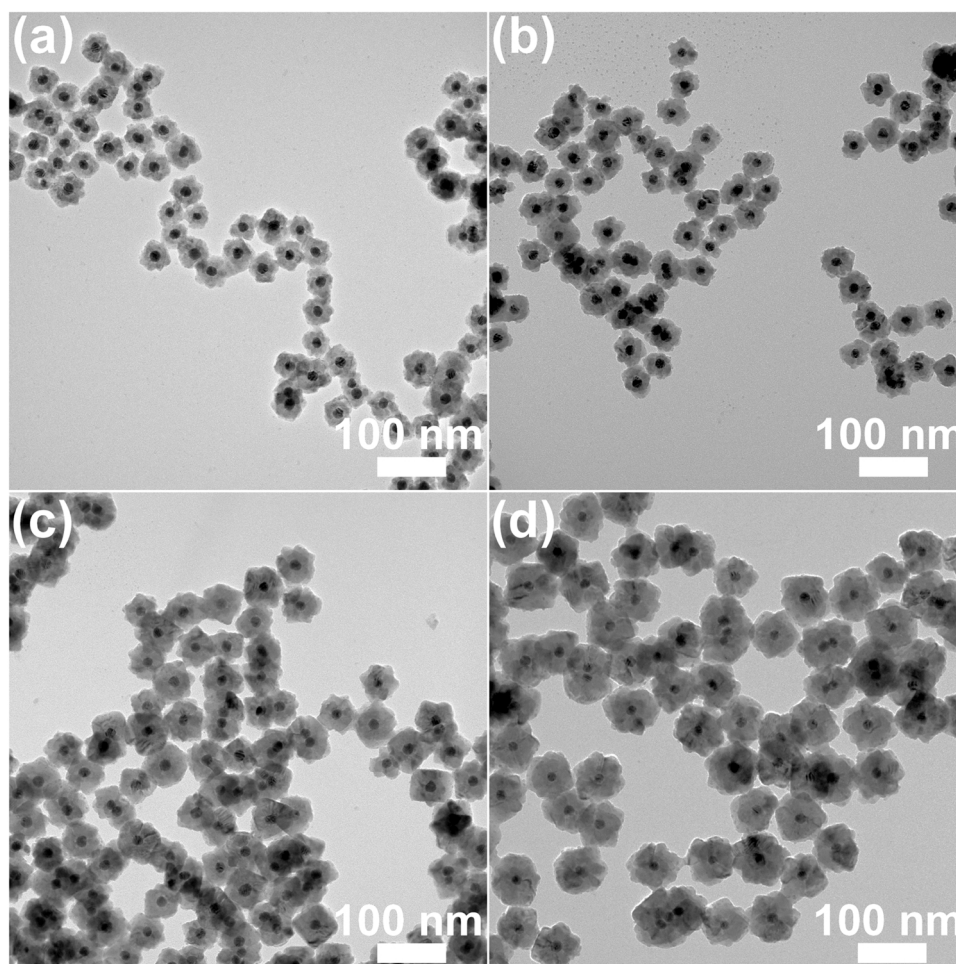


Fig. 1. TEM images of (a) 4-Au@Cu₂O, (b) 3-Au@Cu₂O, (c) 2-Au@Cu₂O and (d) 1-Au@Cu₂O.

the four Au@Cu₂O nanocrystals, pure Au colloids and pure Cu₂O nanocrystals. Two absorption features were noticeable for Au@Cu₂O, consistent with the previous reports [29,31–33]. The broad absorption band at around 660 nm can be ascribed to the surface plasmon resonance (SPR) effect of the composed Au. For aqueous colloidal Au with a size of 15 nm, the reported SPR absorption peak ranges from 520 to 540 nm [32], complying with the spectrum of pure Au colloids. The significant redshift of SPR absorption for Au@Cu₂O originated from the larger refractive index of the Cu₂O shell ($n = 2.3\text{--}3.4$ for Cu₂O [31]) than the surrounding solvent for Au colloids ($n = 1.33$ for water). Note that the SPR absorption of Au can be affected by the refractive index of the surrounding medium and the thickness of the neighboring dielectric [33]. The increasing extent of SPR redshift for Au@Cu₂O with increasing Cu₂O shell thickness can be experimentally recognized from Fig. 3(b) if examined closely. In addition to the SPR absorption, a prominent absorption edge extending to the whole visible and UV regions was also recorded on Au@Cu₂O. Similar absorption edge can be found in pure Cu₂O, which can be assigned to the electronic transition of Cu₂O component with an estimated optical bandgap of 2.2 eV.

3.2. Electronic interactions and band structure

The current Au@Cu₂O nanocrystals represented a typical metal/metal oxide heterogeneous catalyst system that possessed many fascinating properties associated with the electronic interactions between the metal and the surrounding metal oxide. These unique properties can usher the use of Au@Cu₂O catalysts for effective dehydrogenation of AB. Specifically, the charge transfer between Au and Cu₂O can generate

surface charge heterogeneity. The localized charges can activate the adsorbed AB by means of electron redistribution along the B-N bonds [34,35]. The thus-elongated B-N bonds were more inclined to dissociation for proceeding with the subsequent hydrolysis of BH₃. On the other hand, the localized charges can facilitate the extraction of H₂ from one H atom of BH₃ group and the other H atom of H₂O [23,36–38], thereby ensuring the complete liberation of H₂. To study the electronic interactions between Au and Cu₂O, the samples were analyzed with XPS. Fig. 4 shows a comparison of XPS spectra among Au@Cu₂O, pure Au and pure Cu₂O. A noticeable divergence in binding energy was revealed, which can be ascribed to the occurrence of interfacial charge transfer. For Au 4f spectra, the Au@Cu₂O showed a positive binding energy shift of around 0.2 eV compared to pure Au. The positive binding energy shift implied a decrease in electron density for Au core of Au@Cu₂O, presumably a result of electron transfer from Au to Cu₂O. This contention can be supported by the complementary negative binding energy shift observed for Cu₂O shell of Au@Cu₂O. For Cu 2p and O 1s spectra, negative binding energy shifts (0.1 eV for Cu 2p and 0.3 eV for O 1s) were noticed for Au@Cu₂O in comparison with pure Cu₂O. An increase in electron density for Cu₂O shell can account for such negative binding energy shifts, corresponding well with the suggested scenario of electron transfer from Au to Cu₂O. Based on the above results, electronic interactions between Au and Cu₂O were considered significant, which can induce electron transfer from Au to Cu₂O [39] and give rise to noticeable binding energy shifts for Au@Cu₂O.

To further interpret how such a charge transfer scenario occurred, UPS measurements were carried out to construct the band structure for Au@Cu₂O. Fig. 5(a) and (b) show the UPS spectra recorded on pure

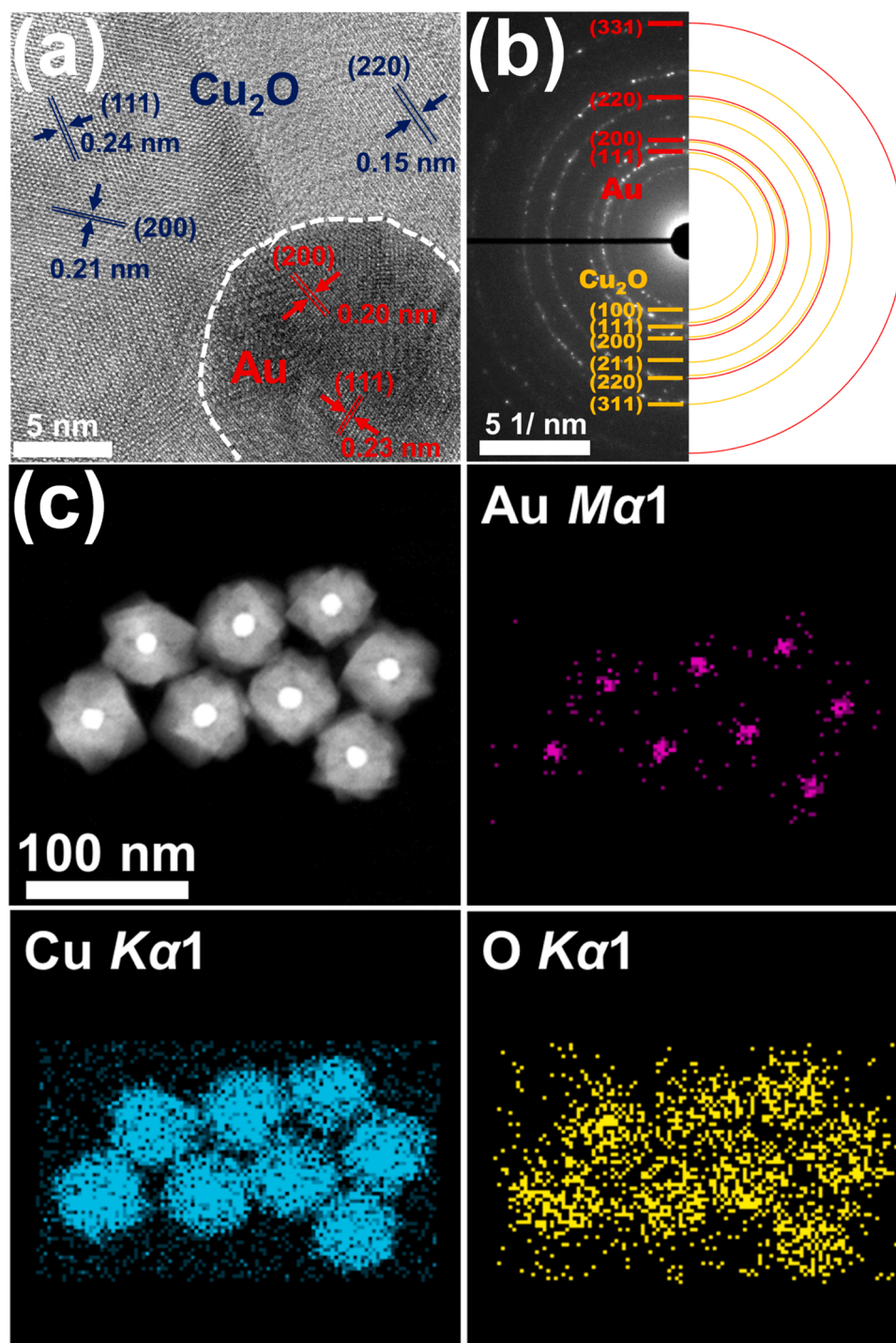


Fig. 2. (a) HRTEM image, (b) SAED pattern, (c) STEM-HAADF image and TEM-EDS mapping plots for 2-Au@Cu₂O.

Cu₂O at the high-energy region and at the region close to 0 eV, respectively. The spectrum at the high-energy region revealed a cut-off energy of 16.42 eV. Here, the cut-off energy represents the difference between the incident photon energy (21.22 eV) and the work function of the sample. By subtracting the cut-off energy from the incident photon energy, the apparent work function of pure Cu₂O can be computed as 4.80 eV. The spectrum at the region close to 0 eV, on the other hand, involves information on the valence band level (E_{VB}) of the sample. By applying a linear extrapolation along the tangent of the onset, the distance of E_{VB} from Fermi level (E_F) can be received, around 0.48 eV for pure Cu₂O. By adding the apparent work function value, the E_{VB} of pure

Cu₂O with respect to the vacuum was determined to be -5.28 eV. Further addition of the optical bandgap can give rise to the conduction band level (E_{CB}) with respect to the vacuum, which was estimated to be -3.08 eV for pure Cu₂O. By using the same calculation procedure, the apparent work function of pure Au can also be obtained from Fig. 5(c), giving an E_F value of -4.29 eV with respect to the vacuum. With these energy levels, a plausible band alignment for Au@Cu₂O was depicted in Fig. 5(d) to interpret the interfacial charge transfer scenario. Note that the measured E_F of pure Cu₂O was fairly close to the E_{VB} level, complying with the p-type semiconductor property of Cu₂O crystal. For Au@Cu₂O, as Cu₂O and Au were brought in contact, the higher E_F of Au

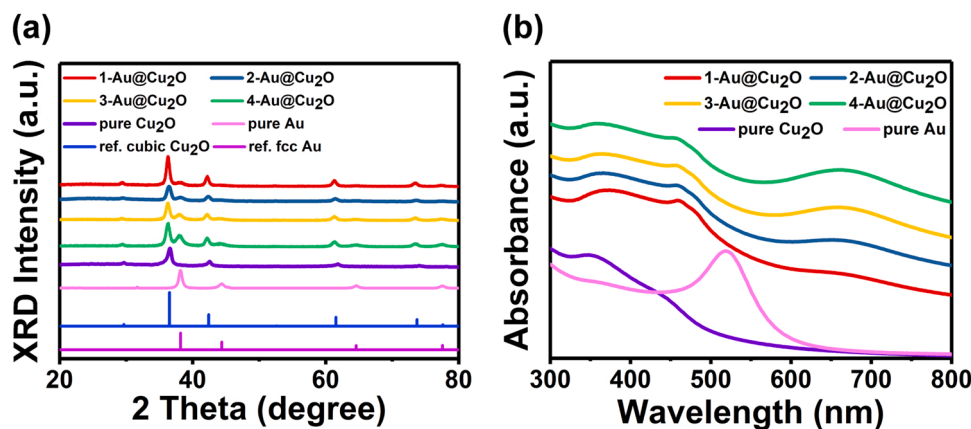


Fig. 3. (a) XRD patterns and (b) UV-visible absorption spectra for the four Au@Cu₂O, pure Au colloids and pure Cu₂O. In (a), the standard patterns of cubic Cu₂O (JCPDS #77-0199) and fcc Au (JCPDS #65-2870) were also included.

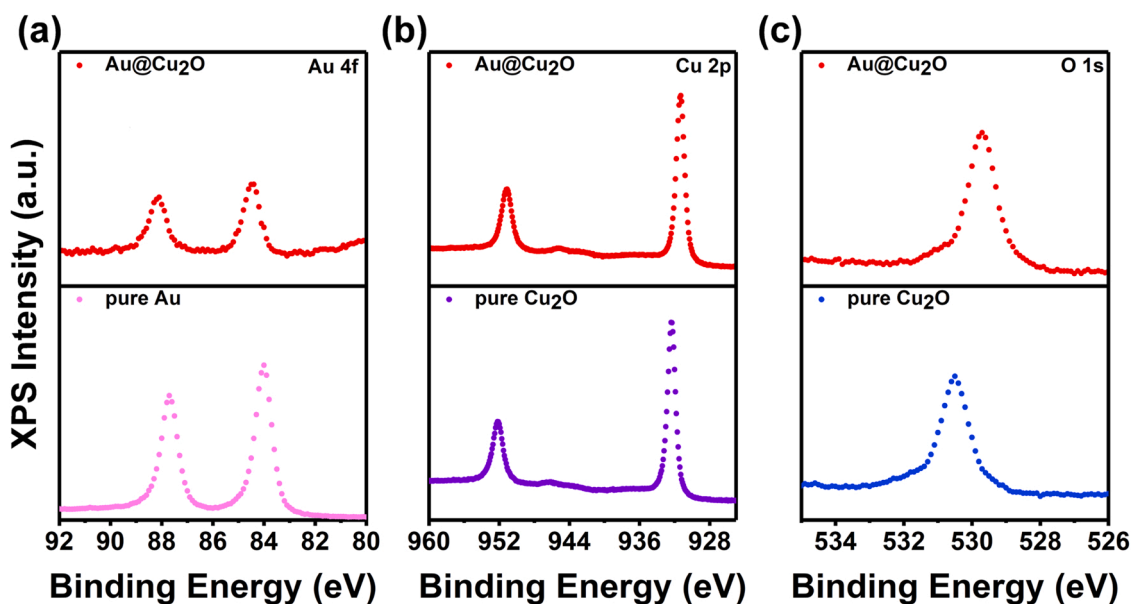


Fig. 4. XPS spectra for 2-Au@Cu₂O, pure Au and pure Cu₂O: (a) Au 4f, (b) Cu 2p, (c) O 1s core levels.

would induce electron transfer from Au to Cu₂O in order to align the E_F of Cu₂O. The electron concentration was therefore accumulated at the interface near the Cu₂O side, accompanied by a downward bending of band edge in the Cu₂O as a result of the depletion of holes. An electron-rich region then developed within the Cu₂O shell. The above argument can be substantiated by examining the apparent E_F level for Au@Cu₂O. As an electron-rich region developed, the E_F level of Cu₂O component of Au@Cu₂O would be lifted. Fig. 6(a) presents the UPS spectra for the four Au@Cu₂O collected at the high-energy region. A cut-off energy of 16.71, 16.72, 16.74 and 16.65 eV were determined for 4-Au@Cu₂O, 3-Au@Cu₂O, 2-Au@Cu₂O and 1-Au@Cu₂O, respectively, giving an apparent E_F value of -4.51 , -4.50 , -4.48 and -4.57 eV vs. vacuum. As expected, all the four Au@Cu₂O showed a lifted E_F in comparison with pure Cu₂O ($E_F = -4.80$ eV vs. vacuum). This observation verified the development of an electron-rich state within the Cu₂O shell for the current Au@Cu₂O. Another important feature obtained from Fig. 6(a) was the variation of the apparent E_F level of Au@Cu₂O with the shell thickness. As the shell thickness increased from 17.0 to 24.5 nm, the apparent E_F level was lifted from -4.51 to -4.48 eV vs. vacuum, achieving the highest level on 2-Au@Cu₂O. Further increasing the shell thickness to 31.5 nm led to an otherwise lowering in the apparent E_F level to -4.57 eV vs. vacuum as observed on 1-Au@Cu₂O. This

phenomenon, depicted in Fig. 6(b), further pointed out that the developed electron-rich state within the Cu₂O shell can be regulated by the shell thickness, which will be later demonstrated to pose a determinant effect on the degree of dehydrogenation of AB over Au@Cu₂O.

3.3. H₂ release from AB hydrolysis

For direct comparison of catalytic performance among Au@Cu₂O with various shell thicknesses, the particle number of each sample was kept a fixed value. To have a fixed particle number (7.63×10^{12}), different amounts of the sample powders were employed to carry out catalytic experiments (see [supplementary material](#) for detailed calculations). Four sets of relevant samples, including Au@Cu₂O with four different shell thicknesses, pure Au colloids, pure Au particle precipitate and pure Cu₂O, were first tested and compared. Fig. 7(a) shows the resultant time course for H₂ release from the hydrolysis of AB. There was no H₂ produced from pure Au particle precipitate, suggesting that the agglomerated Au was inactive toward AB hydrolysis. Pure Au colloids, on the other hand, showed a modicum of activity, releasing 1.0 equivalent of H₂ at a rate of $9.7 \mu\text{mol min}^{-1}$. As compared to pure Au colloids, the four Au@Cu₂O all displayed an increased H₂ production rate along with an enhanced stoichiometric amount of H₂, disclosing the beneficial

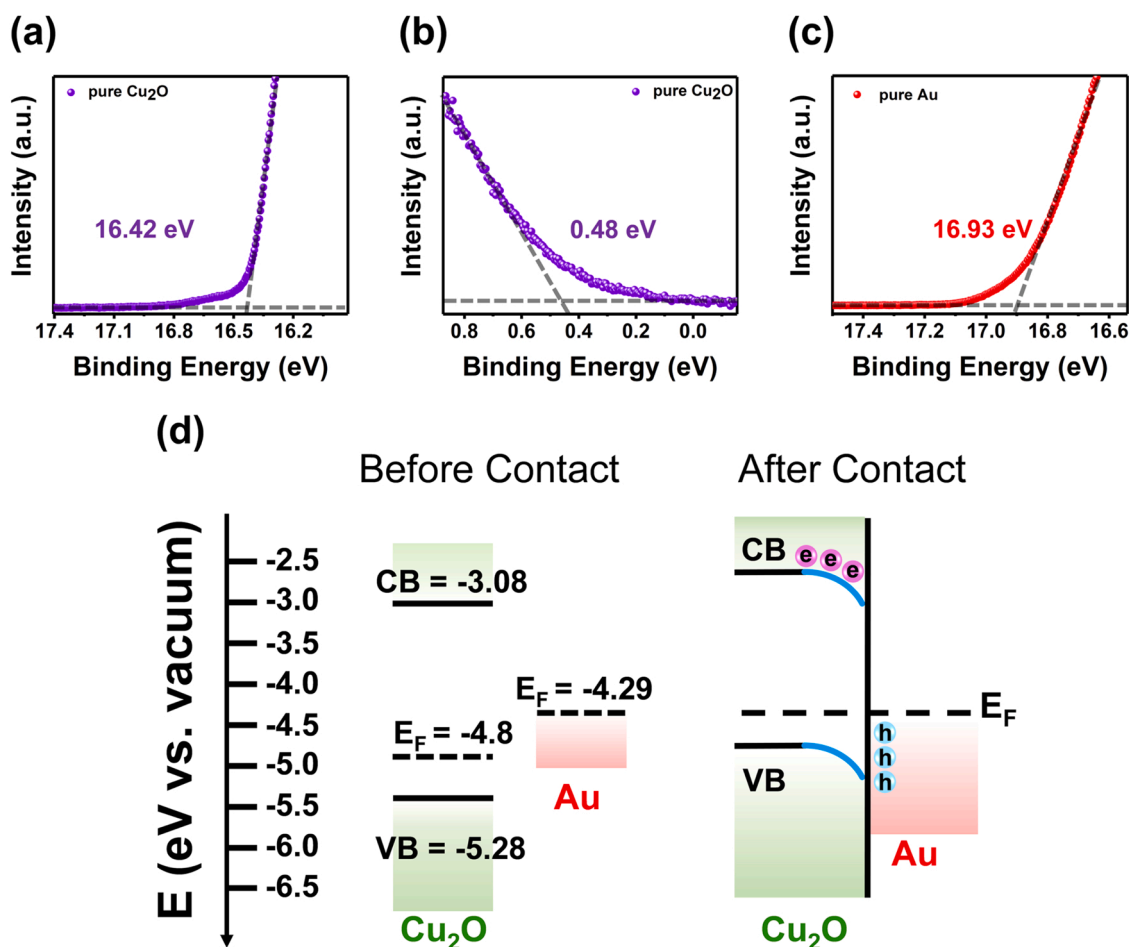


Fig. 5. UPS spectra for (a-b) pure Cu_2O and (c) pure Au. (d) Proposed band alignment for $\text{Au@Cu}_2\text{O}$ before and after contact.

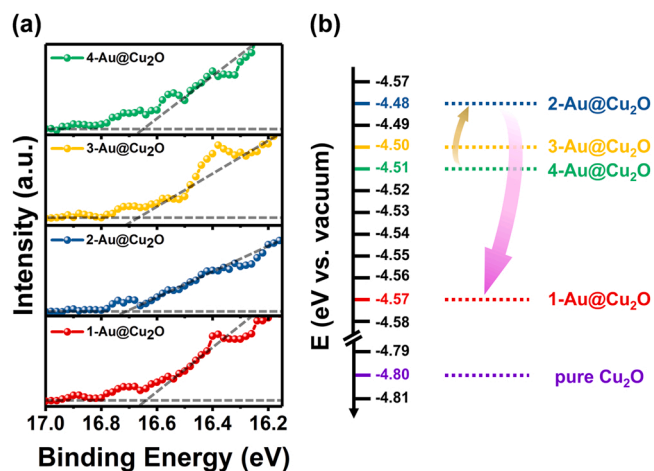


Fig. 6. (a) UPS spectra for the four $\text{Au@Cu}_2\text{O}$ at the high-energy region. (b) Variation of the apparent E_F level of $\text{Au@Cu}_2\text{O}$ with the shell thickness.

function of Cu_2O shell for enhancing the catalytic performance of Au core. For the four $\text{Au@Cu}_2\text{O}$ catalysts, the H_2 production rate increased with increasing shell thickness, reaching 20.5, 28.5, 66.0 and $72.5 \mu\text{mol min}^{-1}$ for 4- $\text{Au@Cu}_2\text{O}$, 3- $\text{Au@Cu}_2\text{O}$, 2- $\text{Au@Cu}_2\text{O}$ and 1- $\text{Au@Cu}_2\text{O}$, respectively. However, the stoichiometric amount of H_2 produced over $\text{Au@Cu}_2\text{O}$ did not monotonically increase with the thickness of Cu_2O . As the shell thickness increased from 17.0 to 19.0 and to 24.5 nm, the stoichiometric amount of H_2 produced increased

accordingly, reaching a maximum of 3.0 equivalents for 2- $\text{Au@Cu}_2\text{O}$. Further increasing the shell thickness to 31.5 nm (1- $\text{Au@Cu}_2\text{O}$) led to an otherwise decrease in the H_2 stoichiometric amount to 2.5 equivalents, even though the H_2 production rate was continuously enhanced. The otherwise decreased stoichiometric amount of H_2 produced over 1- $\text{Au@Cu}_2\text{O}$ disclosed that a counteractive effect was exerted to deteriorate the degree of dehydrogenation of AB as the shell thickness exceeded a critical value, the cause of which will be later explored. Another conspicuous feature seen from Fig. 7(a) was that pure Cu_2O showed a lower H_2 stoichiometric amount (1.8 equivalents) than 2- $\text{Au@Cu}_2\text{O}$, while a comparable H_2 production rate was achieved ($53.0 \mu\text{mol min}^{-1}$). Note that pure Cu_2O shared similar morphology and dimension to 2- $\text{Au@Cu}_2\text{O}$. The lower H_2 stoichiometric amount of pure Cu_2O than that of 2- $\text{Au@Cu}_2\text{O}$ pointed out the necessity of Au particle introduction for promoting the degree of dehydrogenation of AB over Cu_2O . Based on these comparative results, we suggested that Au can cooperate with Cu_2O in a core@shell architecture to achieve effective and complete dehydrogenation of AB. The critical role of core@shell architecture for securing an enhanced activity was further evidenced by assessing the performance of a physical mixture comprising pure Au colloids and pure Cu_2O . As compared in Fig. 7(b), the H_2 production activity of the physical mixture was much lower than 2- $\text{Au@Cu}_2\text{O}$, and even failed to reach the performance of either pure Au colloids or pure Cu_2O . The turnover frequency (TOF), defined by dividing the H_2 production rate by the mole number of the catalyst, was determined to highlight the performance difference. The general form of the calculation formula can be expressed by $\text{TOF} = \frac{n_{\text{H}_2}}{t \times n_{\text{catalyst}}}$, in which n_{H_2} and n_{catalyst} respectively stand for the number of mole of H_2 produced and

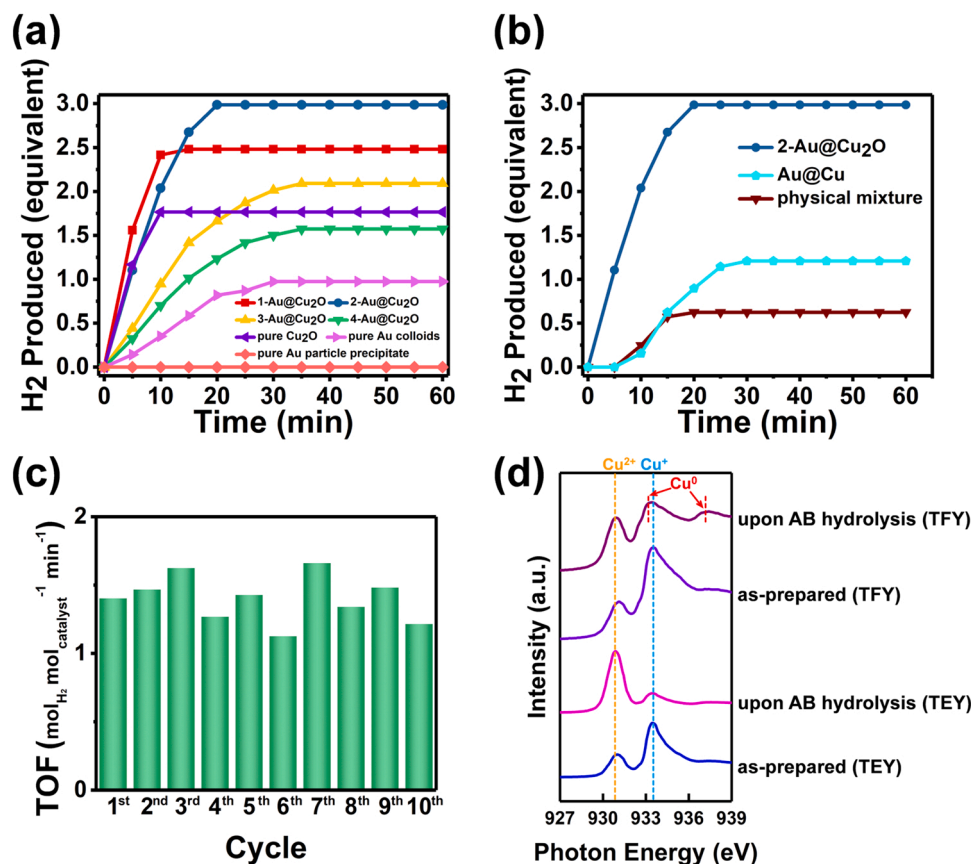


Fig. 7. (a) Time courses for H₂ production from AB hydrolysis over four sets of relevant samples. (b) Comparative results of H₂ production from AB hydrolysis for 2-Au@Cu₂O, physical mixture and Au@Cu. (c) Recycling tests of H₂ production from AB hydrolysis over 2-Au@Cu₂O. (d) Cu L₃-edge XAS spectra in TEY and TFY modes for 2-Au@Cu₂O before and after used in AB hydrolysis.

the number of mole of catalysts loaded, and t is the corresponding reaction time. It is important to mention that n_{catalyst} is estimated based on the amount of the active component in the loaded catalyst. In other words, only the component actually participating in the catalytic reaction is taken into account for the calculation of TOF. Since Cu₂O was considered as the main active sites on Au@Cu₂O, the value of TOF of Au@Cu₂O was determined based on the amount of Cu₂O only, giving a TOF of 1.41 mol_{H₂} mol_{catalyst}⁻¹ min⁻¹ for 2-Au@Cu₂O. For the physical mixture sample, both Au and Cu₂O were exposed to AB molecules and concomitantly participated in the hydrolysis reaction. The n_{catalyst} therefore equated to the total amount of Au and Cu₂O components, giving rise to a TOF of 0.20 mol_{H₂} mol_{catalyst}⁻¹ min⁻¹ for the physical mixture. In addition, an induction period of around 5 min was required for the physical mixture to initiate the hydrolysis reaction. This outcome suggested that simply mixing Au and Cu₂O not only failed to achieve an enhanced activity, but also was subject to retarded reaction kinetics. As Fig. S3(c-d) display, the physical mixture was characteristic of noticeable surface coverage of Cu₂O by the aggregated Au. This microstructural disorder can largely reduce the total number of active sites to cause an interior activity. It should be highlighted that the achievable TOF of 2-Au@Cu₂O was higher than the values of most of the Cu-based catalysts ever reported, as was summarized in Table S2 (supplementary material). Due to the relatively large size, the atom utilization efficiency of the current Au@Cu₂O was considered to be moderate, thus limiting the catalytic performance in terms of TOF. By engineering the structural dimension of Au@Cu₂O, a further increase in TOF can be expected. Besides the H₂ production activity, the stability and recyclability are two other key parameters to demonstrate the practicability of the catalyst toward AB hydrolysis. To evaluate these parameters, 2-Au@Cu₂O was repeatedly used in AB hydrolysis for ten successive cycles. As shown in

Fig. 7(c), the recorded TOF fluctuated during the repeated operation process (TOF = 1.41, 1.43, 1.22 at the 1st, 5th, 10th cycle, respectively). Here, the unsteady TOF of 2-Au@Cu₂O was believed to originate from the occurrence of chemical transformation on the chemically vulnerable Cu₂O component during the AB hydrolysis reaction, instead of the common poisoning-induced deactivation issue. Despite the fluctuation, the achievable maximal TOF can be partly maintained, showing 87% of the initial value at the 10th cycle of operation. The capacity for carrying out complete AB dehydrogenation and maintaining sustainable H₂ production activity demonstrated the robustness of the current Au@Cu₂O in an efficient H₂ release system based on AB hydrolysis.

To further explore the origin behind the fluctuated TOF, we performed XAS measurements to learn the surface and bulk composition of the used Au@Cu₂O. Previous studies have revealed that partial transformation into Cu and Cu(OH)_x can take place on Cu₂O catalysts after the AB hydrolysis reaction [16,40,41]. The occurrence of chemical transformation may alter the catalytic behavior of Au@Cu₂O, possibly affecting the performance of AB hydrolysis. To look into this possibility, the chemical states of 2-Au@Cu₂O before and after used in AB hydrolysis were examined. Here, soft XAS was utilized to identify the chemical states of Cu₂O component because it can provide more reliable fingerprints to recognize different Cu species. Fig. 7(d) summarizes the Cu L₃-edge XAS of 2-Au@Cu₂O before and after AB hydrolysis. Note that the spectra were collected in both TEY and TFY modes to acquire collective information at the surface and in the bulk. The as-prepared, fresh Au@Cu₂O exhibited a minor (931.1 eV) and a major (933.5 eV) absorption peak in both TEY and TFY modes, which can be respectively assigned to Cu²⁺ and Cu⁺ species [42]. The existence of Cu²⁺ species can also be ambiguously designated from the weak satellite peak [43] around 945.3 eV observed in the corresponding Cu 2p XPS spectrum in

Fig. 4(b). This feature suggested that a part of Cu^+ species of the as-prepared $\text{Au@Cu}_2\text{O}$ was oxidized to Cu^{2+} upon exposure to air. After used in AB hydrolysis, the Cu L_3 -edge XAS in TEY mode showed a growth in Cu^{2+} peak intensity and a decay in Cu^+ peak, whereas the spectrum in TFY mode exhibited two additional absorption shoulders associated with metallic Cu. These features indicated that during the process of AB dehydrogenation, the surface Cu^+ of $\text{Au@Cu}_2\text{O}$ was partly oxidized to Cu^{2+} in the form of $\text{Cu}(\text{OH})_2$, while metallic Cu was formed in the shell bulk as a result of the reduction of Cu^+ . Note that the peak position of Cu L_3 -edge for standard $\text{Cu}(\text{OH})_2$ (931.1 eV) and standard CuO (931.4 eV) is distinguishable [44,45], which can be utilized to identify the composition of the partly oxidized surface for the current $\text{Au@Cu}_2\text{O}$. As examined in Fig. 7(d), the absorption peak associated with Cu^{2+} in TEY mode for the used $\text{Au@Cu}_2\text{O}$ was situated at 930.9 eV, fairly approximating to the position of standard $\text{Cu}(\text{OH})_2$. On the other hand, the partly oxidized surface of the used $\text{Au@Cu}_2\text{O}$ was inclined to form Cu(OH)₂ in the alkaline environment during the AB hydrolysis reaction. Further transformation from $\text{Cu}(\text{OH})_2$ into CuO would require an elevated temperature (60 °C) for a prolonged reaction time (20 h) [46], which was improbable to achieve in the current AB hydrolysis reaction system (40 °C for 1 h). According to the above considerations, the composition of the partly oxidized surface of the used $\text{Au@Cu}_2\text{O}$ was presumably $\text{Cu}(\text{OH})_2$. Based on the analytic results of XAS, it can be postulated that during the AB hydrolysis reaction, a part of the Cu_2O shell of $\text{Au@Cu}_2\text{O}$ underwent oxidation and reduction reactions, producing $\text{Cu}(\text{OH})_2$ at the shell surface and metallic Cu in the shell bulk, respectively.

It is important to highlight that the partial chemical transformation into Cu and $\text{Cu}(\text{OH})_2$ did not impart a negative effect on the catalytic activity of $\text{Au@Cu}_2\text{O}$. Note that the $\text{Cu}(\text{OH})_2$ formed at the shell surface can also catalyze AB hydrolysis to release H_2 [47]. In fact, $\text{Cu}(\text{OH})_2$ might be superior to Cu_2O in AB hydrolysis by virtue of the hydroxyl composition [48–50]. This could explain why a slightly increased TOF can be attained by 2-Au@Cu₂O upon the first three cycles of repeated use. The metallic Cu in the shell bulk, on the other hand, can be readily oxidized once it was involved in the succeeding dehydrogenation of AB [17]. This would recover Cu_2O composition in the shell to enable the further repeated usage. The morphology of the used $\text{Au@Cu}_2\text{O}$ was also examined. As displayed in Fig. S5 (supplementary material), the individual $\text{Au@Cu}_2\text{O}$ nanocrystals slightly coalesced after repeatedly used in AB hydrolysis, presumably due to the occurrence of chemical transformation. This minute morphological change did not exert a noticeable negative effect since the used $\text{Au@Cu}_2\text{O}$ can still maintain sustainable H_2 production activity. The findings from XAS analysis however raised an argument on whether a Cu shell combined with an Au core could catalyze AB hydrolysis as efficiently as $\text{Au@Cu}_2\text{O}$ did. To clarify this argument, Au@Cu core@shell nanocrystals were synthesized and tested in AB hydrolysis for comparison. Here, the synthesis of Au@Cu was realized by deliberately conducting chemical reduction on 2-Au@Cu₂O. As presented in Fig. S6 (supplementary material), the thus-obtained Au@Cu was composed of fcc Au and fcc Cu, and inherited particle morphology of 2-Au@Cu₂O. Compared with 2-Au@Cu₂O, Au@Cu exhibited a much lower activity toward AB hydrolysis, merely releasing 1.2 equivalents of H_2 at a rate of $12.1 \mu\text{mol min}^{-1}$, accompanied by an induction period of 5 min, as can be seen from Fig. 7(b). This comparison further highlighted the superb capability of 2-Au@Cu₂O of achieving complete dehydrogenation of AB for efficient H_2 release without a need of induction period.

3.4. Effect of shell thickness

The performance comparison among $\text{Au@Cu}_2\text{O}$ with various shell thicknesses disclosed that a counteractive effect emerged and deteriorated the degree of dehydrogenation of AB as the shell thickness exceeded a critical value. It should be noted that the particle number of the four $\text{Au@Cu}_2\text{O}$ samples was kept a fixed value for conducting the

catalytic experiments. Because of this experimental setup, an increase in shell thickness would give rise to an enlarged area of the exposed surface for individual $\text{Au@Cu}_2\text{O}$ nanocrystals. In other words, a larger shell thickness can endow $\text{Au@Cu}_2\text{O}$ with more accessible surfaces to AB hydrolysis. The apparent surface area of the four $\text{Au@Cu}_2\text{O}$ can be calculated from the BET data, giving 733.50, 847.50, 1270.68, 2075.02 cm^2 for 4-Au@Cu₂O, 3-Au@Cu₂O, 2-Au@Cu₂O and 1-Au@Cu₂O, respectively (see supplementary material for detailed calculations). For AB hydrolysis over $\text{Au@Cu}_2\text{O}$, the surface Cu^+ was considered as main adsorption sites for AB molecules [16]. As increasing the shell thickness, the total number of Cu^+ species at the $\text{Au@Cu}_2\text{O}$ surface was expected to increase. The larger number of Cu^+ species for the thicker $\text{Au@Cu}_2\text{O}$ can therefore bring forth enhanced reaction kinetics of AB hydrolysis. This phenomenon could explain why a maximal H_2 production rate can be attained by 1-Au@Cu₂O, the sample with the largest shell thickness. The enhanced reaction kinetics of AB hydrolysis for $\text{Au@Cu}_2\text{O}$ with increasing shell thickness can also be corroborated by measuring the corresponding activation energy (E_a). The apparent E_a value can be evaluated by performing catalytic experiments under different temperatures (T). The resultant data were displayed in Fig. S7 (supplementary material). Fig. 8(a) shows the Arrhenius plots for the four $\text{Au@Cu}_2\text{O}$ samples. Here, the rate constant (k) of AB hydrolysis was numerically equal to the H_2 production rate as zero-order kinetics with respect to AB concentration was considered [51,52]. The apparent E_a values were estimated from the slopes of the Arrhenius plots, giving 47.6, 43.3, 32.0 and 28.4 kJ/mol for 4-Au@Cu₂O, 3-Au@Cu₂O, 2-Au@Cu₂O and 1-Au@Cu₂O, respectively. As expected, a decrease in E_a was found for $\text{Au@Cu}_2\text{O}$ with increasing shell thickness. This outcome confirmed that the enlarged number of Cu^+ species for $\text{Au@Cu}_2\text{O}$ with increasing shell thickness can facilitate reaction kinetics of AB hydrolysis, leading to the continually increased H_2 production rate. As compared in Table S2 (supplementary material), the E_a attained by 1-Au@Cu₂O ($E_a = 28.4 \text{ kJ/mol}$) was lower than the values of most of the Cu-based catalysts ever reported (E_a ranging from 23.8 to 51.8 kJ/mol). As noted in Table S3 (supplementary material), the achievable E_a of the current $\text{Au@Cu}_2\text{O}$ was also comparable to other recently reported sophisticated catalysts (E_a ranging from 18.96 to 59.7 kJ/mol).

On the other hand, the electronic interactions between Au and Cu_2O and their non-monotonic dependence on the shell thickness posed a significant influence on the degree of dehydrogenation of AB. As deduced from XPS analysis, electron transfer from Au to Cu_2O occurred within $\text{Au@Cu}_2\text{O}$, which can create an electron accumulation (or hole depletion) region at the interface near the Cu_2O side. For $\text{Au@Cu}_2\text{O}$ with a sufficiently thin shell, the electron accumulation region may span across the shell, establishing an electron-rich state at the shell surface. Such a surface electron-rich state not only can activate the BH_3 group of the adsorbed AB [34,35], but also can stimulate the cleavage of O-H bond of the approaching H_2O [23,36–38], facilitating the generation of Cu-H species at the surface of $\text{Au@Cu}_2\text{O}$ to liberate H_2 . The existence of the surface electron-rich state can explain the superiority of 2-Au@Cu₂O over pure Cu_2O in the stoichiometric amount of H_2 produced (3.0 equivalents of H_2 produced over 2-Au@Cu₂O vs. 1.8 equivalents of H_2 produced over pure Cu_2O). At the regime of sufficiently thin shell thickness, the electron accumulation region can be extended across the thickened shell. This would gradually strengthen the surface electron-rich state to result in a progressive increase in the H_2 stoichiometric amount, which reached its peak at 2-Au@Cu₂O. As the shell thickness exceeded a critical value, the established electron accumulation region cannot occupy the whole Cu_2O shell because the localized electrons were difficult to diffuse over a long distance. This would weaken the electron-rich state at the shell surface, as can be inferred from the otherwise lowered E_F level observed for 1-Au@Cu₂O. Note that the sustained generation of Cu-H species at the surface of $\text{Au@Cu}_2\text{O}$ was prerequisite for achieving complete dehydrogenation of AB. The weakened electron-rich state at the shell surface for 1-Au@Cu₂O would

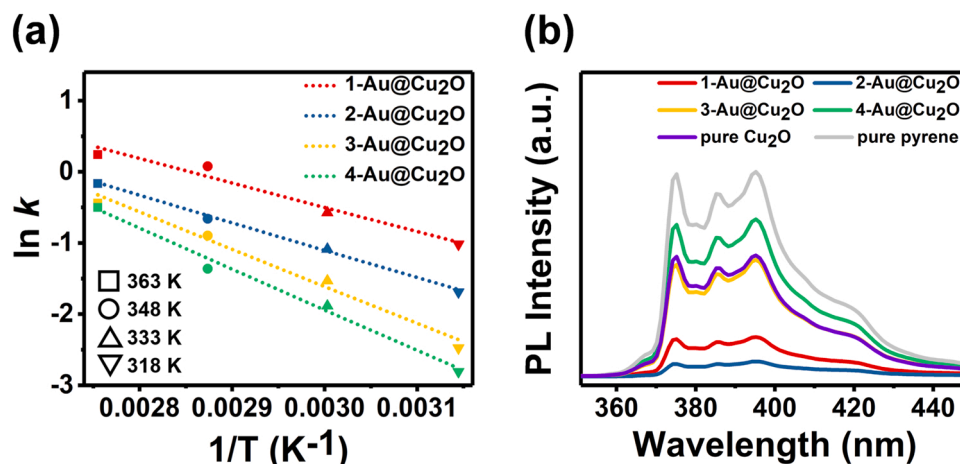


Fig. 8. (a) Arrhenius plots of the four Au@Cu₂O obtained from the H₂ production data. (b) PL spectra of pyrene in the presence of pure Cu₂O and the four Au@Cu₂O.

obstruct the generation of Cu-H species, leading to an otherwise decrease in the stoichiometric amount of H₂ produced.

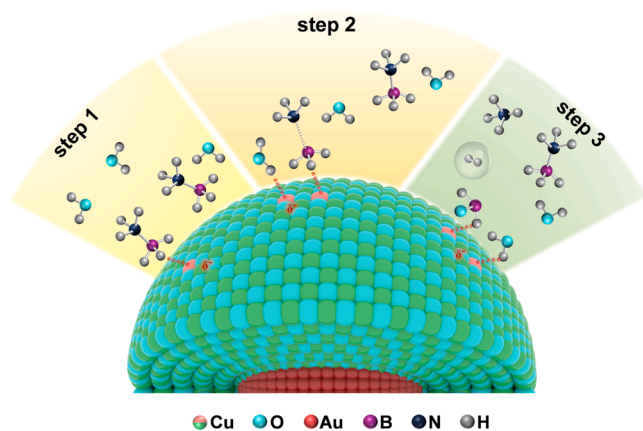
The counteractive effect exerted by the excessive shell thickness can also be examined from the PL quenching experiments by using pyrene as the probe fluorophore. Note that the PL of pyrene can be effectively quenched in the presence of a suitable electron acceptor. Importantly, the energy gap between the lowest unoccupied molecular orbital (LUMO) levels of pyrene and the electron acceptor governs the rate of electron transfer [53]. A reduced energy gap can give rise to an increased rate of electron transfer, thus increasing the extent of PL quenching [54]. By monitoring the extent of PL quenching of pyrene, the electronic state of the selected electron acceptor can be realized. Here, the PL quenching of pyrene was employed to compare the electronic state among the four Au@Cu₂O. Because the CB level of Cu₂O (−3.08 eV vs. vacuum) was less cathodic than the LUMO of pyrene (−1.5 eV vs. vacuum) [54], the photoinduced electrons from the excited pyrene can transfer to Cu₂O and cause a quenched PL for pyrene. Fig. 8(b) shows the PL spectra of pyrene in the presence of five relevant samples. Two important features can be underlined. First, the extent of PL quenching by 2-Au@Cu₂O was higher than that by pure Cu₂O, suggesting that 2-Au@Cu₂O attracted more photoinduced electrons from the excited pyrene than pure Cu₂O did. Because of the Fermi level alignment, the apparent CB level of 2-Au@Cu₂O would be elevated, showing a more cathodic value than that of pure Cu₂O. The elevated CB level would reduce the energy difference from the LUMO of pyrene, thus increasing the extent of PL quenching as observed. The elevated CB level of 2-Au@Cu₂O was consistent with the argument of the existence of the surface electron-rich state, which was believed to be the decisive factor promoting the degree of dehydrogenation of AB. Second, among the four Au@Cu₂O, 2-Au@Cu₂O showed the largest extent of PL quenching. For Au@Cu₂O with sufficiently thin shells (i.e. 4-Au@Cu₂O, 3-Au@Cu₂O and 2-Au@Cu₂O), the extent of PL quenching increased with increasing shell thickness. Since electron accumulation region kept spanning across these thin shells, the apparent CB level would be gradually elevated to lead to a reduced energy difference from the LUMO of pyrene. As such, a progressive increase in the extent of PL quenching resulted. For 1-Au@Cu₂O, the apparent CB level however descended because the electron accumulation region no longer can span across such an excessively thick shell. This contention can be corroborated by the observed lowered E_F level depicted in Fig. 6(b). An enlarged energy difference from the LUMO of pyrene then led to the otherwise reduced extent of PL quenching for 1-Au@Cu₂O. This finding verified the proposed weakened surface electron-rich state for 1-Au@Cu₂O and its contribution to the reduced degree of dehydrogenation of AB.

3.5. Examination of ammonia liberation

It might be argued that ammonia could be liberated from AB hydrolysis to poison Au@Cu₂O and thereby deteriorate the H₂ production activity. Previous reports on sophisticated catalysts design have seldom examined the course of ammonia liberation, as summarized in Table S3 (supplementary material). To clarify the doubt, the compositions of gas and liquid products from AB hydrolysis over 2-Au@Cu₂O were analyzed. In Fig. S8(a) (supplementary material), the FTIR was employed to analyze the liberated NH₃ from the gas product, giving a stoichiometric amount of 0.15 equivalent (relative to 1.0 equivalent of AB). This extent of NH₃ liberation was considerably low as compared to the 3.0 equivalent of H₂ released under the same experimental conditions. Meanwhile, the concentration of the generated NH₄⁺ in the liquid product was also determined by using the colorimetric indophenol blue method [30]. As shown in Fig. S8(b) (supplementary material), a stoichiometric amount of 0.87 equivalent of NH₄⁺ was recorded, illustrating that the ammonia group of AB mostly exited as ammonium form upon dehydrogenation. Importantly, the nearly unity equivalent from the addition of the detected NH₃ and NH₄⁺ validated the chemical integrity for the dehydrogenation of AB over Au@Cu₂O. On the other hand, the surface chemical states of 2-Au@Cu₂O after repeatedly used in AB hydrolysis were inspected with XPS to examine if the catalyst surface was poisoned by ammonium and borate. As revealed in Fig. S9 (supplementary material), no distinguishable peaks assignable to N 1s and B 1s core levels can be observed on the used 2-Au@Cu₂O. This observation, together with the result of recycling tests in Fig. 7(c), suggested that the current Au@Cu₂O was not subject to significant activity poisoning by the residual species from the dehydrogenated AB.

3.6. Mechanism of AB hydrolysis on Au@Cu₂O

In combination with the above analytical results, we proposed a plausible mechanism to interpret the course of H₂ production from AB hydrolysis over Au@Cu₂O in Scheme 1. Considering the fact that Cu₂O was more active than Au toward the dehydrogenation of AB (53.0 $\mu\text{mol min}^{-1}$ and 1.8 equivalents of H₂ produced for pure Cu₂O vs. 9.7 $\mu\text{mol min}^{-1}$ and 1.0 equivalents of H₂ produced for pure Au colloids), we supposed that Cu₂O provided the main active sites for AB hydrolysis on Au@Cu₂O. Specifically, the Cu⁺ species at the surface of Au@Cu₂O can bind to the hydridic H of BH₃ group of AB to form activated complex (step 1), which has been recognized as the rate-determining step of AB hydrolysis [16,55]. Upon attacked by H₂O, concerted dissociation of B-N bonds occurred, leaving BH₃ intermediates [55] at the Au@Cu₂O surface (step 2). Hydrolysis reaction then proceeded by extracting one H atom from BH₃ and the other H atom from



Scheme 1. Plausible mechanism for the course of H_2 production from AB hydrolysis over $\text{Au@Cu}_2\text{O}$.

H_2O , thereby liberating H_2 molecule (step 3). As the shell thickness increased, the total number of Cu^+ species at the $\text{Au@Cu}_2\text{O}$ surface increased. The enriched Cu^+ species would facilitate the interaction of $\text{Au@Cu}_2\text{O}$ with AB, promoting the formation of activated complex to enhance the reaction kinetics. A continuous increase in H_2 production rate along with a concomitant decrease in apparent E_a with shell thickness then resulted. On the other hand, the electronic interactions between Au and Cu_2O can regulate the degree of the dehydrogenation of AB, which can be optimized by means of shell thickness control. For $\text{Au@Cu}_2\text{O}$, the Fermi level equilibrium between Au and Cu_2O caused the establishment of an electron-rich state (δ^-) at the shell surface. This surface electron-rich state can facilitate the generation of Cu-H species and promote the stoichiometric amount of H_2 produced. Under a sufficiently thin shell thickness condition (4-Au@ Cu_2O , 3-Au@ Cu_2O and 2-Au@ Cu_2O), the surface electron-rich state was strengthened with shell thickness, which was reflected from the continuously lifting of E_F level depicted in Fig. 6(b). A progressive increase in the H_2 stoichiometric amount was therefore attained, reaching a maximal 3.0 equivalents of H_2 production for 2-Au@ Cu_2O . In the situation of excessive shell thickness (1-Au@ Cu_2O), the surface electron-rich state would be compromised, which can be identified from the otherwise lowering in the E_F level. Because of the much thickened Cu_2O shell, electron transfer from Au to Cu_2O was presumably limited, resulting in a weakened surface electron-rich state for 1-Au@ Cu_2O . The generation of Cu-H species was obstructed, leading to an otherwise decrease in the H_2 stoichiometric amount as observed for 1-Au@ Cu_2O . As Scheme 1 illustrates, these factors worked together in determining the overall catalytic behavior of $\text{Au@Cu}_2\text{O}$ toward AB hydrolysis. In this work, two activity indexes, i.e. the H_2 production rate and the stoichiometric amount of H_2 produced, were considered and discussed. For H_2 production rate, it increased monotonically with shell thickness, achieving a maximal value on 1-Au@ Cu_2O . Because the particle number of the four $\text{Au@Cu}_2\text{O}$ was maintained identical for conducting AB hydrolysis, an increase in shell thickness gave rise to an enlarged apparent surface area and therefore an increased number of active sites (surface Cu^+ species). As a result of the continuously incremental active sites, a maximal H_2 production rate can be attained by 1-Au@ Cu_2O , the sample with the largest shell thickness. For the stoichiometric amount of H_2 produced, it first increased with the shell thickness, reached a maximum 3.0 equivalents on 2-Au@ Cu_2O , and then decreased as the shell thickness further grew. Note that the stoichiometric amount of H_2 produced from AB hydrolysis was highly related to the degree of dehydrogenation of AB, which was demonstrated to be directly associated with the surface electron-rich state established by electron transfer from Au to Cu_2O . For the samples with a sufficiently thin shell thickness (4-Au@ Cu_2O , 3-Au@ Cu_2O and 2-Au@ Cu_2O), the surface electron-rich state was

strengthened with shell thickness, reaching the most pronounced for 2-Au@ Cu_2O to release a maximal 3.0 equivalents of H_2 . For the sample with an excessive shell thickness (1-Au@ Cu_2O), the surface electron-rich state would be compromised because of the limited electron transfer from Au to Cu_2O . An otherwise decrease in the stoichiometric amount of H_2 produced was therefore observed on 1-Au@ Cu_2O .

3.7. Practical use for powering

To demonstrate the application scenario, the H_2 produced from AB hydrolysis over $\text{Au@Cu}_2\text{O}$ was fed directly into a customized H_2 -air fuel cell (cell output = 1 W) to generate electricity for lightening of light emitting diodes (LEDs). The experimental setup was depicted in Fig. 9 (a). In this demonstration, a given amount of 2-Au@ Cu_2O was used to catalyze the hydrolysis of 0.65 mmol AB in an airtight flask, which produced 1.95 mmol H_2 in 20 min with an ideal energy output of 557.7 J. During the catalytic process, the produced H_2 was transported to the fuel cell by a deliver tube. The fuel cell was connected to a 5 mm LED on a breadboard through the circuits. As displayed in Fig. 9(b-d), three LEDs were separately tested, including red, yellow and green. Once H_2 was evolved from the reaction solution, the connected LEDs were immediately lighted. As measured by a digital multimeter, the current and voltage required to light a red LED was 16 mA and 1.83 V, respectively, corresponding to a power of 29.28 mW. By conducting one batch experiment of AB hydrolysis over 2-Au@ Cu_2O , the produced H_2 can supply power to light a red LED for over 5.0 h. As to the yellow and green LEDs, the required power for lighting was 29.42 and 33.55 mW, respectively. By utilizing the produced H_2 , the yellow and green LEDs can be continuously powered for 5.0 and 4.5 h, respectively. This demonstration highlighted the great promise of the current $\text{Au@Cu}_2\text{O}$ as practical catalysts in H_2 production from AB hydrolysis for utilization in portable fuel cells.

4. Conclusions

The practical use of $\text{Au@Cu}_2\text{O}$ as sustainable catalysts for efficient H_2 production from AB hydrolysis was demonstrated. The surface Cu^+ of $\text{Au@Cu}_2\text{O}$ was considered as main adsorption sites for AB molecules, which dictated the reaction kinetics of AB hydrolysis to determine the H_2 production rate. As increasing the shell thickness, the total number of Cu^+ species at the $\text{Au@Cu}_2\text{O}$ surface increased, bringing forth enhanced reaction kinetics to give rise to a continuously increased H_2 production rate. On the other hand, the electronic interactions between Au and Cu_2O and their non-monotonic dependence on the shell thickness posed a significant influence on the degree of dehydrogenation of AB. For $\text{Au@Cu}_2\text{O}$ with a sufficiently thin shell, the electron accumulation region can be extended across the thickened shell, gradually strengthening the surface electron-rich state to result in a progressive increase in the H_2 stoichiometric amount. A maximal 3.0 equivalents of H_2 production was achieved by 2-Au@ Cu_2O , the sample with an optimal Cu_2O shell thickness of 24.5 nm. As the shell thickness exceeded a critical value, the established electron accumulation region cannot occupy the whole Cu_2O shell, leading to a weakened electron-rich state at the shell surface. An otherwise decrease in the H_2 stoichiometric amount to 2.5 equivalents was thereby observed for 1-Au@ Cu_2O , the sample with the largest shell thickness of 31.5 nm. By considering the proposed structural regulation and electronic engineering principles as guidelines, one can construct a versatile catalyst platform comprising metals and metal oxides for robust H_2 production from AB hydrolysis. The present study also discloses a promising step toward the utilization of the catalytically released H_2 in the fuel cell-based H_2 economy.

CRedit authorship contribution statement

Mei-Jing Fang conducted materials synthesis and measurements, analyzed all the data, and drafted the manuscript. Yu-Chang Lin

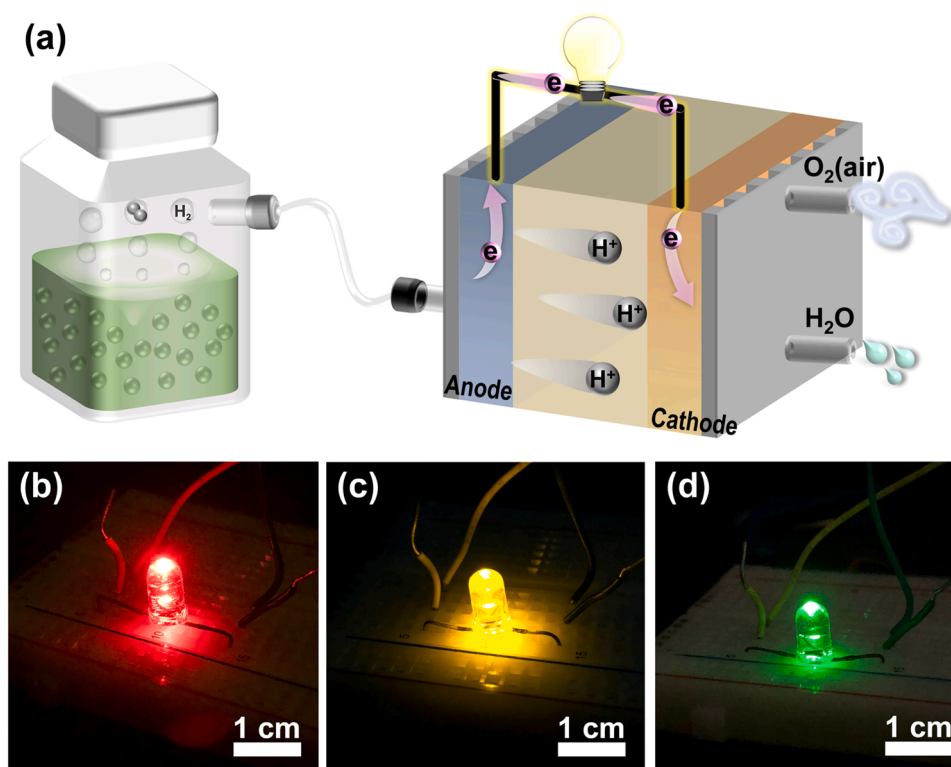


Fig. 9. (a) Schematic experimental setup for utilizing the H_2 produced from AB hydrolysis over $\text{Au@Cu}_2\text{O}$ to power a H_2 -air fuel cell for lighting of LEDs. (b-d) Pictures showing the lighted red, yellow and green LEDs.

conducted XAS measurements and data analysis. **Jen-Yu Jan** conducted FTIR measurements and data analysis. **Ting-Hsuan Lai** provided insightful comments on data interpretation. **Ping-Yen Hsieh** provided insightful comments on data interpretation. **Ming-Yu Kuo** provided insightful comments on data interpretation. **Yi-Hsuan Chiu** provided insightful comments on data interpretation. **Chun-Wen Tsao** provided insightful comments on data interpretation. **Yi-An Chen** provided insightful comments on data interpretation. **Yu-Ting Wang** provided insightful comments on data interpretation. **Yi-Jia Hong** provided insightful comments on data interpretation. **Jhen-Yang Wu** provided insightful comments on data interpretation. **Yew Chung Sermon Wu** provided insightful comments on data interpretation. **Yan-Gu Lin** provided insightful comments on data interpretation. **Tso-Fu Mark Chang** provided insightful comments on data interpretation. **Chun-Yi Chen** provided insightful comments on data interpretation. **Masato Sone** provided insightful comments on data interpretation. **Sue-Min Chang** provided insightful comments on data interpretation. **Chung-Liang Chang** provided insightful comments on data interpretation. **Yung-Jung Hsu** conceived the idea of the project, reviewed, and edited the manuscript.

Data Availability

No data was used for the research described in the article.

Acknowledgements

This work was financially supported by the Ministry of Science and Technology (MOST) of Taiwan under grants MOST 108-2628-M-009-004-MY3, MOST 108-2218-E-009-039-MY3, and MOST 109-2923-M-009-003-MY2, and by the National Science and Technology Council under grant MOST 111-2113-M-A49-038. This work was also supported by National Science and Technology Council, Taiwan (grant No. NSTC 111-2634-F-A49-007) and the Center for Emergent Functional Matter

Science of National Yang Ming Chiao Tung University from The Featured Areas Research Center Program within the framework of the Higher Education Sprout Project by the Ministry of Education (MOE) in Taiwan. This work was supported in part by the World Research Hub (WRH) Program of the International Research Frontiers Initiative at Institute of Innovative Research, Tokyo Institute of Technology. The assistance of Ching-Wen Tsai from the Instrumentation Center at National Tsing Hua University for UPS measurements, Ying-Mei Chang from the Instrumentation Center at National Tsing Hua University for STEM measurements, and Hsiu-Yin Huang from the Instrumentation Resource Center at National Yang Ming Chiao Tung University for XPS and FE-SEM analysis is also appreciated.

Declaration of competing interest

The authors declare no competing interests.

Appendix A. Supporting information

Supplementary data associated with this article can be found in the online version at [doi:10.1016/j.apcatb.2022.122198](https://doi.org/10.1016/j.apcatb.2022.122198).

References

- [1] J. Graetz, New Approaches to Hydrogen Storage, *Chem. Soc. Rev.* 38 (2009) 73–82, <https://doi.org/10.1039/B718842K>.
- [2] X. Yu, Z. Tang, D. Sun, L. Ouyang, M. Zhu, Recent Advances and Remaining Challenges of Nanostructured Materials for Hydrogen Storage Applications, *Prog. Mater. Sci.* 88 (2017) 1–48, <https://doi.org/10.1016/j.pmatsci.2017.03.001>.
- [3] M. Zhang, X. Xiao, Y. Wu, Y. An, L. Xu, C. Wan, Hydrogen Production from Ammonia Borane over PtNi Alloy Nanoparticles Immobilized on Graphite Carbon Nitride, *Catalysts* 9 (2019) 1009, <https://doi.org/10.3390/catal9121009>.
- [4] A. Staubitz, A.P. Robertson, I. Manners, Ammonia-Borane and Related Compounds as Dihydrogen Sources, *Chem. Rev.* 110 (2010) 4079–4124, <https://doi.org/10.1002/9783527629800.ch8>.
- [5] Q. Xu, M. Chandra, A Portable Hydrogen Generation System: Catalytic Hydrolysis of Ammonia-Borane, *J. Alloy. Compd.* 446 (2007) 729–732, <https://doi.org/10.1016/j.jallcom.2007.01.040>.

- [6] H.L. Jiang, Q. Xu, Catalytic Hydrolysis of Ammonia Borane for Chemical Hydrogen Storage, *Catal. Today* 170 (2011) 56–63, <https://doi.org/10.1016/j.cattod.2010.09.019>.
- [7] M. Chandra, Q. Xu, A High-Performance Hydrogen Generation System: Transition Metal-Catalyzed Dissociation and Hydrolysis of Ammonia-Borane, *J. Power Sources* 156 (2006) 190–194, <https://doi.org/10.1016/j.jpowsour.2005.05.043>.
- [8] S. Basu, A. Brockman, P. Gagare, Y. Zheng, P. Ramachandran, W. Delgass, J. Gore, Chemical Kinetics of Ru-Catalyzed Ammonia Borane Hydrolysis, *J. Power Sources* 188 (2009) 238–243, <https://doi.org/10.1016/j.jpowsour.2008.11.085>.
- [9] S. Akbayrak, Y. Tonbul, S. Ozkar, Ceria Supported Rhodium Nanoparticles: Superb Catalytic Activity in Hydrogen Generation from the Hydrolysis of Ammonia Borane, *Appl. Catal. B* 198 (2016) 162–170, <https://doi.org/10.1016/j.apcatb.2016.05.061>.
- [10] S. Rej, C.F. Hsia, T.Y. Chen, F.C. Lin, J.S. Huang, M.H. Huang, Facet-Dependent and Light-Assisted Efficient Hydrogen Evolution from Ammonia Borane Using Gold–Palladium Core–Shell Nanocatalysts, *Angew. Chem.-Int. Edit.* 128 (2016) 7338–7342, <https://doi.org/10.1002/ange.201603021>.
- [11] J.W. Park, S.W. Lai, S.O. Cho, Catalytic Hydrogen Generation from Hydrolysis of Ammonia Borane Using Octahedral Au@Pt Nanoparticles, *Int. J. Hydrog. Energy* 40 (2015) 16316–16322, <https://doi.org/10.1016/j.ijhydene.2015.09.119>.
- [12] M. Zhu, Y. Dai, W. Fu, Y. Wu, X. Zou, T. You, Y. Sun, Novel Photocatalyst Gold Nanoparticles with Dumbbell-Like Structure and Their Superior Photocatalytic Performance for Ammonia Borane Hydrolysis, *Nanotechnology* 29 (2018), 165707, <https://doi.org/10.1088/1361-6528/aaabff>.
- [13] Z.H. Lu, J. Li, A. Zhu, Q. Yao, W. Huang, R. Zhou, R. Zhou, X. Chen, Catalytic Hydrolysis of Ammonia Borane via Magnetically Recyclable Copper Iron Nanoparticles for Chemical Hydrogen Storage, *Int. J. Hydrog. Energy* 38 (2013) 5330–5337, <https://doi.org/10.1016/j.ijhydene.2013.02.076>.
- [14] O. Ozay, E. Inger, N. Aktas, N. Sahiner, Hydrogen Production from Ammonia Borane via Hydrogel Template Synthesized Cu, Ni, Co Composites, *Int. J. Hydrog. Energy* 36 (2011) 8209–8216, <https://doi.org/10.1016/j.ijhydene.2011.04.140>.
- [15] L. Zhou, T. Zhang, Z. Tao, J. Chen, Ni Nanoparticles Supported on Carbon as Efficient Catalysts for the Hydrolysis of Ammonia Borane, *Nano Res.* 7 (2014) 774–781, <https://doi.org/10.1007/s12274-014-0438-7>.
- [16] S.B. Kalidindi, U. Sanyal, B.R. Jagirdar, Nanostructured Cu and Cu@Cu₂O Core Shell Catalysts for Hydrogen Generation from Ammonia–Borane, *Phys. Chem. Chem. Phys.* 10 (2008) 5870–5874, <https://doi.org/10.1039/B805726E>.
- [17] Y. Yamada, K. Yano, Q. Xu, S. Fukuzumi, Cu/Co₃O₄ Nanoparticles as Catalysts for Hydrogen Evolution from Ammonia Borane by Hydrolysis, *J. Phys. Chem. C* 114 (2010) 16456–16462, <https://doi.org/10.1021/jp104291s>.
- [18] W. Chen, W. Fu, G. Qian, B. Zhang, D. Chen, X. Duan, X. Zhou, Synergistic Pt-WO₃ Dual Active Sites to Boost Hydrogen Production from Ammonia Borane, *iScience* 23 (2020), 100922, <https://doi.org/10.1016/j.isci.2020.100922>.
- [19] J. Qi, J. Chen, G. Li, S. Li, Y. Gao, Z. Tang, Facile Synthesis of Core–Shell Au@CeO₂ Nanocomposites with Remarkably Enhanced Catalytic Activity for CO Oxidation, *Energy Environ. Sci.* 5 (2012) 8937–8941, <https://doi.org/10.1039/C2EE22600F>.
- [20] Z.H. Lu, H.L. Jiang, M. Yadav, K. Araniishi, Q. Xu, Synergistic Catalysis of Au-Co@SiO₂ Nanospheres in Hydrolytic Dehydrogenation of Ammonia Borane for Chemical Hydrogen Storage, *J. Mater. Chem.* 22 (2012) 5065–5071, <https://doi.org/10.1039/C2JM14787D>.
- [21] W.W. Zhan, Q.L. Zhu, Q. Xu, Dehydrogenation of ammonia borane by metal nanoparticle catalysts, *ACS Catal.* 6 (2016) 6892–6905, <https://doi.org/10.1021/acscatal.6b02209>.
- [22] K. Mori, K. Miyawaki, H. Yamashita, Ru and Ru–Ni Nanoparticles on TiO₂ Support as Extremely Active Catalysts for Hydrogen Production from Ammonia–Borane, *ACS Catal.* 6 (2016) 3128–3135, <https://doi.org/10.1021/acscatal.6b00715>.
- [23] J. Zhang, Y. Dong, Q. Liu, M. Zhou, G. Mi, X. Du, Hierarchically Alloyed Pd–Cu Microarchitecture with Tunable Shapes: Morphological Engineering, and Catalysis for Hydrogen Evolution Reaction of Ammonia Borane, *Int. J. Hydrog. Energy* 44 (2019) 30226–30236, <https://doi.org/10.1016/j.ijhydene.2019.09.213>.
- [24] M. Asim, S. Zhang, M. Ai, B. Maryam, Y. Wang, X. Li, J. Yang, J.-J. Zou, L. Pan, Photohydrolysis of Ammonia Borane for Effective H₂ Evolution via Hot Electron-Assisted Energy Cascade of Au-WO₂ 72/TiO₂, *Ind. Eng. Chem. Res.* 61 (2022) 11429–11435, <https://doi.org/10.1021/acs.iecr.2c01945>.
- [25] S. Jo, P. Verma, Y. Kuwahara, K. Mori, W. Choi, H. Yamashita, Enhanced Hydrogen Production from Ammonia Borane Using Controlled Plasmonic Performance of Au Nanoparticles Deposited on TiO₂, *J. Mater. Chem. A* 5 (2017) 21883–21892, <https://doi.org/10.1039/C7TA07264C>.
- [26] S. Zhou, Y. Yang, P. Yin, Z. Ren, L. Wang, M. Wei, Metal-Support Synergistic Catalysis in Pt/MoO₃-x Nanorods toward Ammonia Borane Hydrolysis with Efficient Hydrogen Generation, *ACS Appl. Mater. Interfaces* 14 (2022) 5275–5286, <https://doi.org/10.1021/acsami.1c20736>.
- [27] M.Y. Kuo, C.F. Hsiao, Y.H. Chiu, T.H. Lai, M.J. Fang, J.Y. Wu, J.W. Chen, C.L. Wu, K.H. Wei, H.C. Lin, Y.J. Hsu, Au@Cu₂O Core@Shell Nanocrystals as Dual-Functional Catalysts for Sustainable Environmental Applications, *Appl. Catal. B-Environ.* 242 (2019) 499–506, <https://doi.org/10.1016/j.apcatb.2018.09.075>.
- [28] V. Andal, G. Buvaneswari, Effect of Reducing Agents in the Conversion of Cu₂O Nanocolloid to Cu Nanocolloid, *Eng. Sci. Technol.* 20 (2017) 340–344, <https://doi.org/10.1016/j.jestech.2016.09.003>.
- [29] C.H. Kuo, Y.T. Chu, Y.F. Song, M.H. Huang, Cu₂O Nanocrystal-Templated Growth of Cu₂S Nanocages with Encapsulated Au Nanoparticles and In-Situ Transmission X-ray Microscopy Study, *Adv. Funct. Mater.* 21 (2011) 792–797, <https://doi.org/10.1002/adfm.201002108>.
- [30] Y. Wang, X. Cui, J. Zhao, G. Jia, L. Gu, Q. Zhang, L. Meng, Z. Shi, L. Zheng, C. Wang, Rational Design of Fe–N/C Hybrid for Enhanced Nitrogen Reduction Electrocatalysis under Ambient Conditions in Aqueous Solution, *ACS Catal.* 9 (2018) 336–344, <https://doi.org/10.1021/acscatal.8b03802>.
- [31] C. Xiang, G.M. Kimball, R.L. Grimm, B.S. Brunschwig, H.A. Atwater, N.S. Lewis, 820 mV Open-Circuit Voltages from Cu₂O/CH₃CN Junctions, *Energy Environ. Sci.* 4 (2011) 1311–1318, <https://doi.org/10.1039/C0EE00554A>.
- [32] X. Ji, X. Song, J. Li, Y. Bai, W. Yang, X. Peng, Size Control of Gold Nanocrystals in Citrate Reduction: The Third Role of Citrate, *J. Am. Chem. Soc.* 129 (2007) 13939–13948, <https://doi.org/10.1021/ja074447k>.
- [33] J.F. Li, Y.J. Zhang, S.Y. Ding, R. Panneerselvam, Z.Q. Tian, Core–Shell Nanoparticle-Enhanced Raman Spectroscopy, *Chem. Rev.* 117 (2017) 5002–5069, <https://doi.org/10.1021/acs.chemrev.6b00596>.
- [34] B. Wang, L. Xiong, H. Hao, H. Cai, P. Gao, F. Liu, X. Yu, C. Wu, S. Yang, The “Electric-Dipole” Effect of Pt–Ni for Enhanced Catalytic Dehydrogenation of Ammonia Borane, *J. Alloy. Compd.* 844 (2020), 156253, <https://doi.org/10.1016/j.jallcom.2020.156253>.
- [35] P. Verma, K. Yuan, Y. Kuwahara, K. Mori, H. Yamashita, Enhancement of Plasmonic Activity by Pt/Ag Bimetallic Nanocatalyst Supported on Mesoporous Silica in the Hydrogen Production from Hydrogen Storage Material, *Appl. Catal. B* 223 (2018) 10–15, <https://doi.org/10.1016/j.apcatb.2017.05.017>.
- [36] Z. Li, T. He, L. Liu, W. Chen, M. Zhang, G. Wu, P. Chen, Covalent Triazine Framework Supported Non-Noble Metal Nanoparticles with Superior Activity for Catalytic Hydrolysis of Ammonia Borane: From Mechanistic Study to Catalyst Design, *Chem. Sci.* 8 (2017) 781–788, <https://doi.org/10.1039/C6SC02456D>.
- [37] B. Qi, L. Du, F. Yao, S. Xu, X. Deng, M. Zheng, S. He, H. Zhang, X. Zhou, Shape-Controlled Dodecaborate Supramolecular Organic-Framework-Supported Ultrafine Trimetallic PtCoNi for Catalytic Hydrolysis of Ammonia Borane, *ACS Appl. Mater. Interfaces* 11 (2019) 23445–23453, <https://doi.org/10.1021/acsami.9b02963>.
- [38] X. Du, C. Yang, X. Zeng, T. Wu, Y. Zhou, P. Cai, G. Cheng, W. Luo, Amorphous NiP Supported on rGO for Superior Hydrogen Generation from Hydrolysis of Ammonia Borane, *Int. J. Hydrog. Energy* 42 (2017) 14181–14187, <https://doi.org/10.1016/j.ijhydene.2017.04.052>.
- [39] Z. Zhang, R. Song, T. Cao, W. Huang, Morphology-Dependent Structures and Catalytic Performances of Au Nanostructures on Cu₂O Nanocrystals Synthesized by Galvanic Replacement Reaction, *J. Energy Chem.* 25 (2016) 1086–1091, <https://doi.org/10.1016/j.jechem.2016.09.012>.
- [40] Y. Yamada, K. Yano, S. Fukuzumi, Catalytic Application of Shape-Controlled Cu₂O Particles Protected by Cu₃O₄ Nanoparticles for Hydrogen Evolution from Ammonia Borane, *Energy Environ. Sci.* 5 (2012) 5356–5363, <https://doi.org/10.1039/C1EE02639A>.
- [41] Y. Feng, H. Wang, X. Chen, F. Lv, Y. Li, Y. Zhu, C. Xu, X. Zhang, H.R. Liu, H. Li, Simple Synthesis of Cu₂O–CoO Nanoplates with Enhanced Catalytic Activity for Hydrogen Production from Ammonia Borane Hydrolysis, *Int. J. Hydrog. Energy* 45 (2020) 17164–17173, <https://doi.org/10.1016/j.ijhydene.2020.04.257>.
- [42] P. Jiang, D. Prendergast, F. Borondics, S. Porsgaard, L. Giovanetti, E. Pach, J. Newberg, H. Blum, F. Besenbacher, M. Salmeron, Experimental and Theoretical Investigation of the Electronic Structure of Cu₂O and CuO Thin Films on Cu(110) Using X-Ray Photoelectron and Absorption Spectroscopy, *J. Chem. Phys.* 138 (2013), 024704, <https://doi.org/10.1063/1.4773583>.
- [43] X. Ma, J. Zhang, B. Wang, Q. Li, S. Chu, Hierarchical Cu₂O foam/g-C₃N₄ Photocathode for Photoelectrochemical Hydrogen Production, *Appl. Surf. Sci.* 427 (2018) 907–916, <https://doi.org/10.1016/j.apsusc.2017.09.075>.
- [44] L.C. Pardo Pérez, A. Arndt, S. Stojkovic, I.Y. Ahmet, J.T. Arens, F. Dattila, R. Wendt, A. Guilherme Buzanich, M. Radtke, V. Davies, K. Höflich, E. Köhnen, P. Tockhorn, R. Gollak, J. Xiao, G. Schuck, M. Wollgarten, N. López, M.T. Mayer, Determining Structure-Activity Relationships in Oxide Derived Cu–Sn Catalysts During CO₂ Electroreduction Using X-Ray Spectroscopy, *Advanced Energy Materials* 12 (2022) 2103328, <https://doi.org/10.1002/aenm.202103328>.
- [45] K. Shimizu, H. Maeshima, H. Yoshida, A. Satsuma, T. Hattori, Ligand Field Effect on the Chemical Shift in XANES Spectra of Cu(II) Compounds, *Phys. Chem. Chem. Phys.* 3 (2001) 862–866, <https://doi.org/10.1039/B007276L>.
- [46] O. Akhavan, R. Azimrad, S. Safa, E. Hasani, CuO/Cu(OH)₂ Hierarchical Nanostructures as Bactericidal Photocatalysts, *J. Mater. Chem.* 21 (2011) 9634–9640, <https://doi.org/10.1039/C0JM04364H>.
- [47] C.Y. Peng, C.C. Hou, Q.Q. Chen, C.J. Wang, X.J. Lv, J. Zhong, W.F. Fu, C.M. Che, Y. Chen, Cu(OH)₂ Supported on Fe(OH)₃ as a Synergistic and Highly Efficient System for the Dehydrogenation of Ammonia-Borane, *Sci. Bull.* 63 (2018) 1583–1590, <https://doi.org/10.1016/j.scib.2018.11.003>.
- [48] Z.C. Fu, Y. Xu, S.L.F. Chan, W.W. Wang, F. Li, F. Liang, Y. Chen, Z.S. Lin, W.F. Fu, C.M. Che, Highly Efficient Hydrolysis of Ammonia Borane by Anion (–OH, F–, Cl–)-Tuned Interactions between Reactant Molecules and CoP Nanoparticles, *Chem. Commun.* 53 (2017) 705–708, <https://doi.org/10.1039/C6CC08120G>.
- [49] C.C. Hou, Q. Li, C.J. Wang, C.Y. Peng, Q.Q. Chen, H.F. Ye, W.F. Fu, C.M. Che, N. López, Y. Chen, Ternary Ni–Co–P Nanoparticles as Noble-Metal-Free Catalysts to Boost the Hydrolytic Dehydrogenation of Ammonia-Borane, *Energy Environ. Sci.* 10 (2017) 1770–1776, <https://doi.org/10.1039/C7EE01553D>.
- [50] C. Wang, J. Tuninetti, Z. Wang, C. Zhang, R. Ciganda, L. Salmon, S. Moya, J. Ruiz, D. Astruc, Hydrolysis of Ammonia-Borane over Ni/ZIF-8 Nanocatalyst: High Efficiency, Mechanism, and Controlled Hydrogen Release, *J. Am. Chem. Soc.* 139 (2017) 11610–11615, <https://doi.org/10.1021/jacs.7b06859>.
- [51] X. Qiu, X. Wu, Y. Wu, Q. Liu, C. Huang, The Release of Hydrogen from Ammonia Borane over Copper/Hexagonal Boron Nitride Composites, *RSC Adv.* 6 (2016) 106211–106217, <https://doi.org/10.1039/C6RA24000C>.
- [52] L.L. Fu, D.F. Zhang, Z. Yang, T.W. Chen, J. Zhai, PtAuCo Trimetallic Nanoalloys as Highly Efficient Catalysts toward Dehydrogenation of Ammonia Borane, *ACS Sustain. Chem. Eng.* 8 (2020) 3734–3742, <https://doi.org/10.1021/acssuschemeng.9b06865>.

- [53] C.W. Tsao, M.J. Fang, Y.J. Hsu (Eds.), Modulation of Interfacial Charge Dynamics of Semiconductor Heterostructures for Advanced Photocatalytic Applications, *Coord. Chem. Rev.* 438 (2021), 213876, <https://doi.org/10.1016/j.ccr.2021.213876>.
- [54] H.S. Jang, H.S. Cho, D. Uhrig, M.P. Nieh, Insight into the Interactions between Pyrene and Polystyrene for Efficient Quenching Nitroaromatic Explosives, *J. Mater. Chem. C* 5 (2017) 12466–12473, <https://doi.org/10.1039/C7TC04288D>.
- [55] Q. Xu, M. Chandra, Catalytic Activities of Non-Noble Metals for Hydrogen Generation from Aqueous Ammonia-Borane at Room Temperature, *J. Power Sources* 163 (2006) 364–370, <https://doi.org/10.1016/j.jpowsour.2006.09.043>.